


Article

Latonduine-1-Amino-Hydantoin Hybrid, Triazole-Fused Latonduine Schiff Bases and Their Metal Complexes: Synthesis, X-ray and Electron Diffraction, Molecular Docking Studies and Antiproliferative Activity

Christopher Wittmann ¹, Tim Gruene ¹, Alexander Prado-Roller ¹, Sandra Arandelović ²,
Jóhannes Reynisson ³ and Vladimir B. Arion ^{1,*}

¹ Institute of Inorganic Chemistry, University of Vienna, Währinger Strasse 42, A1090 Vienna, Austria

² Institute of Oncology and Radiology of Serbia, Pasterova 14, 11000 Belgrade, Serbia

³ School of Pharmacy and Bioengineering, Keele University, Hornbeam Building, Staffordshire ST5 5BG, UK

* Correspondence: vladimir.arion@univie.ac.at

Abstract: A series of latonduine derivatives, namely 11-nitro-indolo[2,3-*d*]benzazepine-7-(1-amino-hydantoin) (**B**), triazole-fused indolo[2,3-*d*]benzazepine-based Schiff bases **HL**¹ and **HL**² and metal complexes [M(*p*-cymene)(HL¹)Cl]Cl, where M = Ru (**1**), Os (**2**), and [Cu(HL²)Cl₂] (**3**) were synthesized and characterized by spectroscopic techniques (UV-vis, ¹H, ¹³C, ¹⁵N-¹H HSQC NMR) and ESI mass spectrometry. The molecular structures of **B** and **HL**¹ were confirmed by single-crystal X-ray diffraction, while that of **3** by electron diffraction of nanometer size crystalline sample. Molecular docking calculations of species **B** in the binding pocket of PIM-1 enzyme revealed that the 1-amino-hydantoin moiety is not involved in any hydrogen-bonding interactions, even though a good accommodation of the host molecule in the ATP binding pocket of the enzyme was found. The antiproliferative activity of organic compounds **B**, **HL**¹ and **HL**², as well as complexes **1–3** was investigated in lung adenocarcinoma A549, colon adenocarcinoma LS-174 and triple-negative breast adenocarcinoma MDA-MB-231 cells and normal human lung fibroblast cells MRC-5 by MTT assays; then, the results are discussed.

Keywords: indolobenzazepines; antiproliferative activity; ruthenium(II); osmium(II); copper(II)



Citation: Wittmann, C.; Gruene, T.; Prado-Roller, A.; Arandelović, S.; Reynisson, J.; Arion, V.B. Latonduine-1-Amino-Hydantoin Hybrid, Triazole-Fused Latonduine Schiff Bases and Their Metal Complexes: Synthesis, X-ray and Electron Diffraction, Molecular Docking Studies and Antiproliferative Activity. *Inorganics* **2023**, *11*, 30. <https://doi.org/10.3390/inorganics11010030>

Academic Editor: Isabel Correia

Received: 15 November 2022

Revised: 18 December 2022

Accepted: 28 December 2022

Published: 3 January 2023



Copyright: © 2023 by the authors. Licensee MDPI, Basel, Switzerland. This article is an open access article distributed under the terms and conditions of the Creative Commons Attribution (CC BY) license (<https://creativecommons.org/licenses/by/4.0/>).

1. Introduction

In our modern society cancer has become a major threat [1]. Even though more and more people survive this severe disease in some particular cases, such as lung cancer, survival rate did not ameliorate much over the years. Cancer is still the second frequent cause for death after cardiovascular diseases [2]. The Global Cancer Observatory estimates that the total number of incidences and mortality will rise in the nearest future [3]. These predictions make the search for new anticancer drugs even more imperative.

Indolo[3,2-*d*]benzazepines, also known as Paullones (Figure 1), and their metal complexes have been extensively studied over the last two decades. The compounds revealed antiproliferative activities with IC₅₀ values from the low micromolar concentration range down to submicromolar concentrations for Ru(II)- and Os(II)-arene complexes, and even to the nanomolar concentration range for some Cu(II) complexes [4–8]. As possible targets underlying the mechanism of antiproliferative activity of these compounds at the molecular level several cancer related kinases were reported, namely GSK3β, CDK2/cyclin A, Lck and Src [9–17].

Quite recently we turned our attention to indolo[2,3-*d*]benzazepine derivatives as isomers of Paullones. Intriguingly, their backbone is derived from the natural alkaloids of Latonduines (Figure 1), which do not show marked cytotoxicity [18,19]. However,

fusion of an additional indole moiety to the Latonduine skeleton led to an enormous enhancement of antiproliferative activity with IC_{50} values in the low to sub-micromolar concentration range [20]. The favorable effect of an indole core on the pharmacological profile of other drugs is well-documented in the literature [21–23]. These indolo[2,3-*d*]benzazepine molecules were discovered to act as microtubule destabilizing agents (MDA) fitting well into the colchicine binding pocket [24]. One disadvantage for the development of these molecules as anticancer drugs is their poor aqueous solubility. As for Paullones this drawback could be overcome by their coordination to metals via creation of suitable binding sites attached to the main scaffold (see Figure 2) [4,5,7,8,25]. Ru(II)- and Os(II)-arene, as well as Cu(II) complexes with these potential indolo[2,3-*d*]benzazepine ligands shown in Figure 2 were recently prepared and investigated for their antiproliferative activity [26–28].

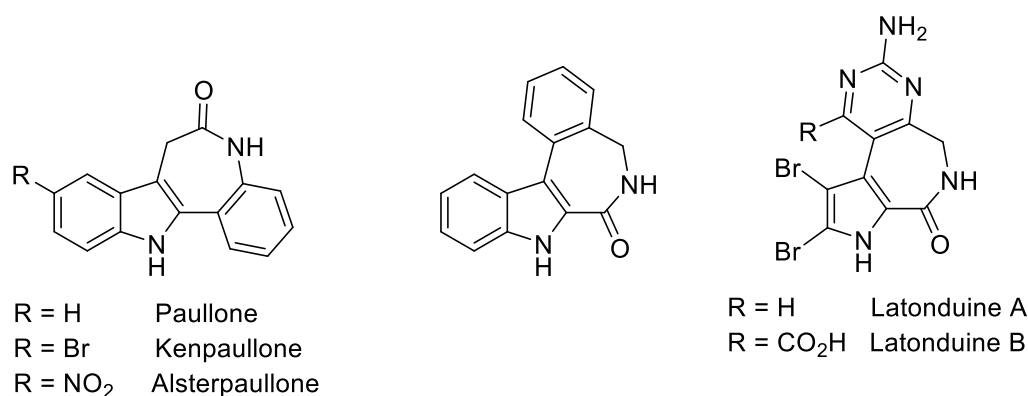


Figure 1. Line drawings of indolo[3,2-*d*]benzazepines (Paullones), indolo[2,3-*d*]benzazepine and Latonduines.

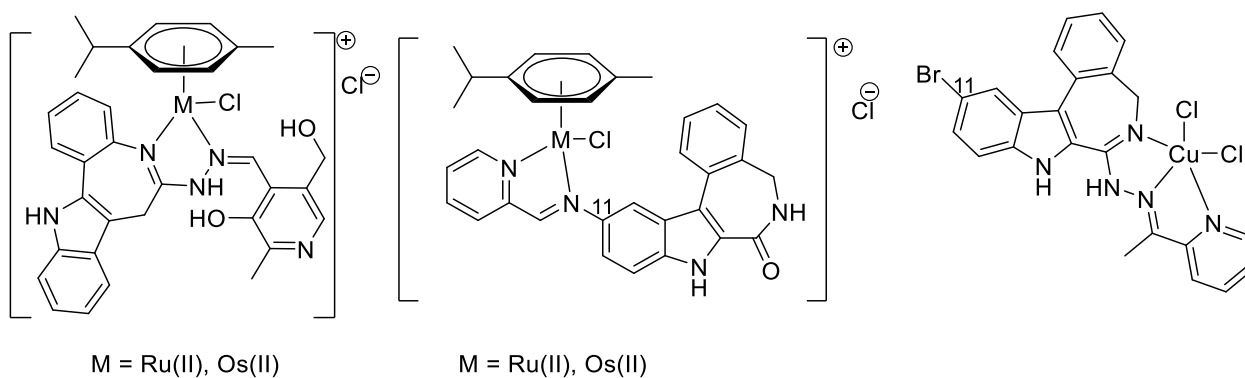


Figure 2. From left to right: Ru(II)/Os(II) complexes with Paullone and Latonduine derivatives with different binding sites, and a Cu(II) complex with a Latonduine modified at the lactam moiety.

Established structure-activity relationships (SARs) revealed very good antiproliferative activity of the metal-free Latonduine derivatives modified at the lactam moiety [27,28], while those containing a metal-binding unit at position 11 (Figure 2) are markedly less active, but still with IC_{50} values in the micromolar concentration range [26]. In both cases metal complex formation with the respective transition metals enhanced the pharmacological profile, however, distinct differences could still be observed. For Cu(II) complexes the aqueous solubility only slightly increased, while cytotoxicity of lead compounds reached the low nanomolar concentration range [27,28]. Cationic Ru(II) and Os(II) complexes became soluble in biocompatible media, but IC_{50} values did not ameliorate when compared to those of metal-free derivatives [26]. Taking into account the established SARs, and, in particular, that the increase in the cytotoxicity of indolo[2,3-*d*]benzazepines is observed when structural modifications are performed at the lactam moiety of the backbone (compare with [26,27]), as well as the results reported by Anand et al. [29] on the synthesis of a large

library of MST1 kinase inhibitors via coupling of inert organoruthenium complexes with bioactive fragments, we selected one of them, namely, 1-amino-hydantoin (1-AH, see Figure 3 highlighted in blue) as a unit to be attached to our scaffold at the lactam group (see Figure 3). We expected to increase the docking ability of the new hybrid to ATP binding sites of cancer related mammalian kinases, and eventually enhance their antiproliferative activity [29].

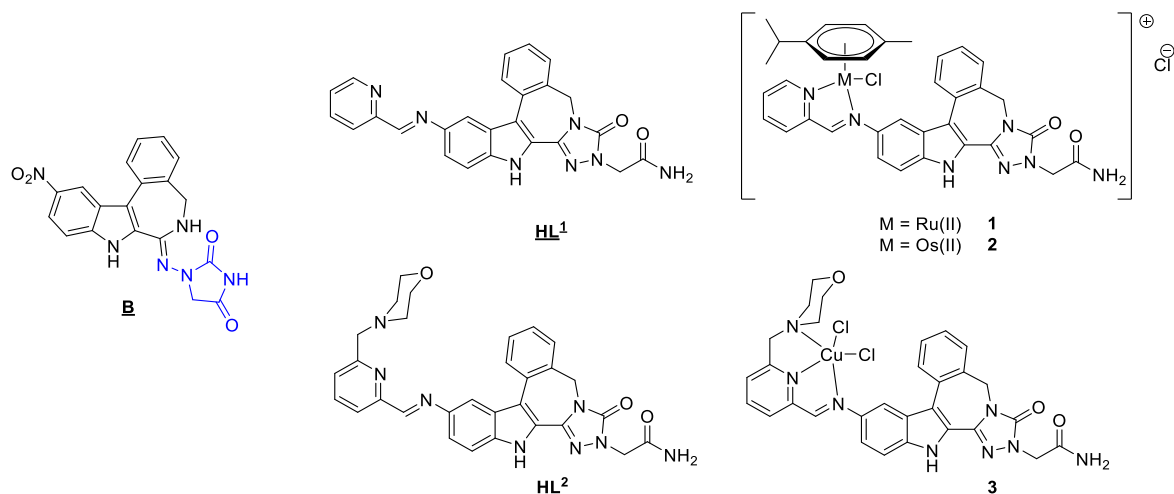


Figure 3. Core structure **B** (1-AH moiety is highlighted in blue), ligands **HL¹** and **HL²**, and their Ru(II)- and Os(II)-arene, as well as Cu(II) complexes **1–3**. Underlined numbers indicate compounds studied by SC-XRD or ED methods.

Transition metal complexes of hydantoin derivatives are known [30] and positive effects of hydantoin on antimitotic and antiviral activities of inactive amino acids were reported [31]. In addition, this moiety has been proven to have an immunomodulating effect antagonizing carcinogenesis [32] and its derivatives can act as independent EGFR-inhibitors and inducers of apoptosis [33,34] providing further arguments in favor of using this 1-AH unit for the design of new anticancer drugs.

Herein we report on attempts to attach the 1-AH unit at the lactam moiety of 11-nitroindolo[2,3-*d*]benzazepine-7-one and create a suitable binding site at position 11 for accommodation of Ru(II)/Os(II) and Cu(II). The prepared two ligands (**HL¹** and **HL²**) along with Ru(II)- and Os(II)-*p*-cymene, and Cu(II) complexes **1–3** collected in Figure 3 were spectroscopically (¹H, ¹³C NMR, 2D NMR, UV-vis) characterized and their structures confirmed by ESI mass spectrometry and single-crystal X-ray diffraction (SC-XRD), as well as by Electron Diffraction (ED), a new technique, which was used for determination of the structure of the nanometer size crystals. All compounds were assessed for antiproliferative activity and structure-activity relationships were discussed.

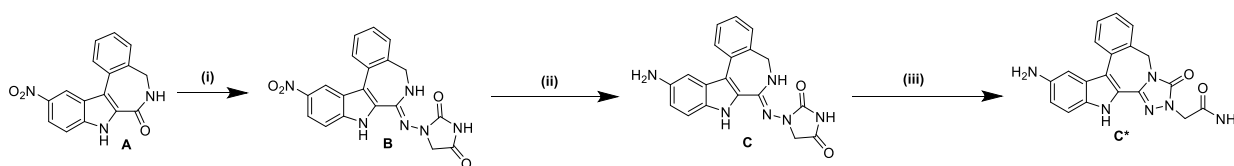
2. Results and Discussion

2.1. Synthesis and Spectroscopic Analysis

The synthesis of potential ligands **HL¹** and **HL²** started with attempts to couple 1-AH to scaffold **A** at the lactam moiety. As thiolactam group is considered to be more suitable for condensation reaction with hydrazine monohydrate [27,28], we tried first to thionate species **A**. The reaction of **A** with P₄S₁₀ afforded the thiolactam derivative in low yield. However, further reaction with 1-AH failed, and species **B** could not be prepared. When **A** was allowed to react with an excess POCl₃ at reflux under inert atmosphere a more reactive 7-chloroimine derivative was generated, a species already reported previously for indoloquinolines [6,25,35]. Further reaction with excess 1-AH in dry MeCN produced compound **B**, which was isolated as hydrochloride salt. The hydrochloride in EtOAc was neutralized with a saturated aqueous solution of sodium bicarbonate to give the free base.

Purification on silica resulted in the desired product of excellent purity and moderate yield (60%). Positive ion ESI mass spectrum revealed a peak with m/z 391.17 attributed to $[M+H]^+$ (calcd m/z 391.12). A single-crystal X-ray diffraction structure of species **B** confirmed the attachment of 1-AH moiety to the main scaffold (*vide infra*).

Further reduction in **B** with molecular hydrogen in the presence of Pd/C at 3 bar in dry THF [26] yielded pure amine **C** in almost quantitative yield. Condensation of amine **C** bearing 1-AH moiety with pyridine-2-carboxaldehyde and 2-formyl-6-morpholinomethylpyridine was expected to afford Schiff bases bearing the same 1-AH moiety. However, spectroscopic (^1H , ^{13}C and ^{15}N - ^1H HSQC NMR) investigation of analytically pure products **HL**¹ and **HL**² indicated the formation of unexpected species via intramolecular ring closure reaction, which is facilitated in the presence of base. Suspending **C** in methanol with a small amount of NEt_3 and stirring at reflux for 3 h resulted in cyclization product **C*** (see Scheme 1). The typical chemical shift for H^5 (~10.9 ppm) in Latonduines [26–28] in ^1H NMR spectra of **B** and **C** disappeared in the case of **C*** (see Figures S4–S6). Upon Schiff-base condensation of **C** with the two aldehydes to **HL**¹ and **HL**², respectively, this singlet disappeared as well (see Figures S7 and S8), indicating a similar transformation with that of **C** into **C***. In addition, ^{15}N - ^1H HSQC NMR spectra revealed two new protons of the amide group further attesting the identity of **HL**¹ and **HL**² (see Figure S15). Positive ion ESI mass spectra of **HL**¹ and **HL**² showed peaks with m/z 472.22 and 549.33 attributed to $[M+\text{Na}]^+$ and $[M+H]^+$, respectively. The molecular structure of the compounds was further confirmed by single-crystal X-ray diffraction study of **HL**¹ (*vide infra*).



Scheme 1. Synthesis pathway for core amine **C**. (i): (1) POCl_3 , $130\text{ }^\circ\text{C}$, 3 h, (2) 1-AH, MeCN, $50\text{ }^\circ\text{C}$, 16 h; (ii): Pd/C (10%), THF, H_2 , 3 bar, RT, 28 h; (iii): NEt_3 , MeOH, reflux, 3 h.

The synthesis of metal(II)-arene complexes **1** and **2** was performed by reactions of **HL**¹ with $[\text{MCl}_2(p\text{-cymene})]_2$ ($\text{M} = \text{Ru}, \text{Os}$) in hot isopropanol as reported for other related complexes elsewhere [26]. ESI mass spectra of **1** and **2** revealed peaks with m/z 720.21 and 810.26, respectively, which could be easily assigned to $[\text{M}(p\text{-cymene})(\text{HL}^1)\text{Cl}]^+$, where $\text{M} = \text{Ru}$ and Os . The experimental isotopic patterns for these ions were in very good agreement with calculated isotopic distributions (see Supplementary Material). Complex **3** was synthesized by reaction of **HL**² with $\text{CuCl}_2 \cdot 2\text{H}_2\text{O}$ in boiling isopropanol as recently reported for similar compounds [27,28]. The ESI mass spectrum of **3** showed a peak with m/z 646.20, which could be assigned to $[\text{Cu}(\text{HL}^2)\text{Cl}]^+$ (calcd m/z 646.13). If the structure of diamagnetic complexes **1** and **2** could be confirmed by ^1H and ^{13}C NMR spectra, the coordination geometry of copper(II) in complex **3** could not be inferred directly from ESI mass spectrometry investigation or elemental analysis. Attempts to obtain single crystals of X-ray diffraction quality for routine measurements failed. However, investigation of the powdered sample under electronic microscope (see Experimental part) showed the presence of very small crystals of 100 nm size, which proved to be suitable for collection of electron diffraction (ED) data, structure solution and refinement. The results of ED study of complex **3** and X-ray diffraction measurements of species **B** and ligand **HL**¹ are discussed below.

Elemental analyses of **B**, **HL**¹, **HL**² and **1–3** (Table S1 in the Supplementary Material) confirmed their $\geq 95\%$ purity required for *in vitro* testing.

2.2. Molecular Structure Description of Species **B**, **HL**¹ and **3**

The results of X-ray diffraction measurements of species **B** and potential ligand **HL**¹ are shown in Figure 4, while those of the electron diffraction structure of complex **3** in Figure 5. Details of data collection and refinement are summarized in Table S2.

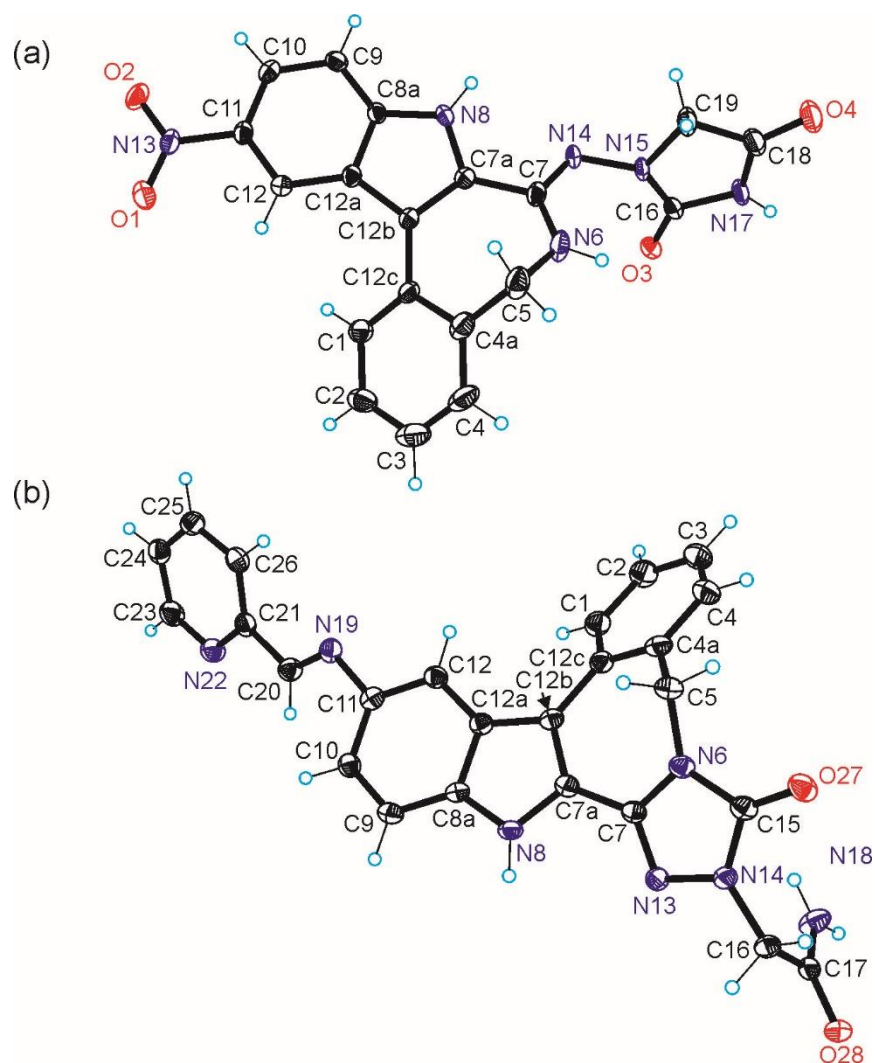


Figure 4. (a) ORTEP view of **B** with thermal ellipsoids at 50% probability level. Selected bond distances (Å) and torsion angles (deg): N6–C7 1.339(3), C7–C7A 1.460(7), C7–N14 1.318(3), N14–N15 1.417(2), C16–O3 1.213(2), C18–O4 1.221(3), $\Theta_{C7-N14-N16-C16}$ 97.8(2), $\Theta_{O1-N13-C11-C12}$ 4.6(3); (b) ORTEP view of **HL**¹ with thermal ellipsoids at 50% probability level. Selected bond distances (Å), bond angles (deg) and torsion angles (deg): C5–N6 1.462(2), N6–C7 1.367(2), C7–C7A 1.444(2), C7–N13 1.307(2), N13–N14 1.3911(19), N14–C15 1.378(2), N6–C15 1.384(2), C16–N17 1.359(4), $\Theta_{C4a-C5-N6-C7}$ –62.7(2).

Species **B** crystallized in the monoclinic centrosymmetric space group $C2/c$, **HL**¹ in the centrosymmetric triclinic space group $P\bar{1}$, while complex **3** in the monoclinic centrosymmetric space group $P2_1/n$.

Complex **3** adopts a slightly distorted square-pyramidal coordination geometry ($\tau_5 = 0.07$) [36]. The Schiff base acts as a neutral tridentate ligand **HL**² binding to copper(II) via azomethine nitrogen atom N19, the pyridine nitrogen N22 and morpholine nitrogen atom N28 and together with the chlorido co-ligand C11 forms the base of the pyramid. The apical position is occupied by the second chlorido co-ligand Cl2.

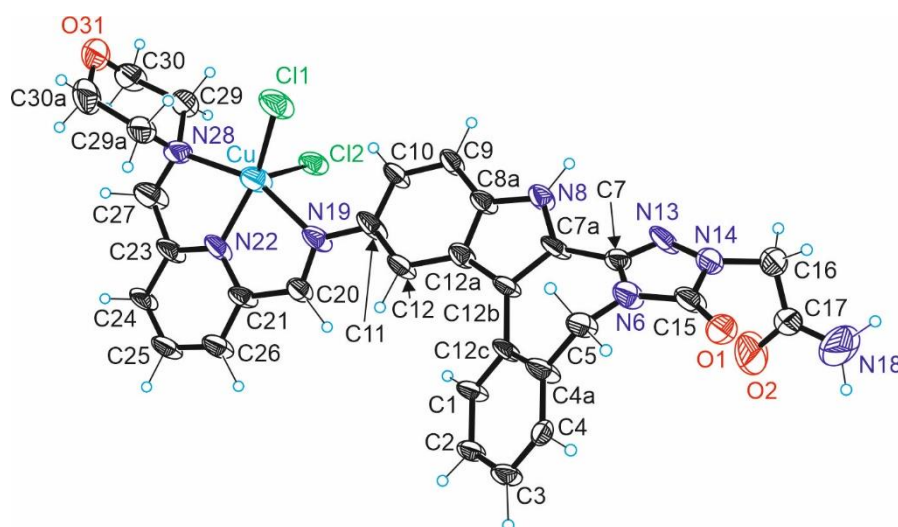


Figure 5. Electron Diffraction (ED) structure of complex **3** with thermal ellipsoids at 40% probability level. Selected bond distances (Å): Cu–N19 2.162(12), Cu–N22 1.932(7), Cu–N28 2.223(13), Cu–Cl1 2.282(8), Cu–Cl2 2.223(13) Å.

2.3. Stability in Solution

To confirm solution stability of the compounds to be tested *in vitro* for their antiproliferative activity 1% aqueous DMSO solutions of complexes **1–3** were monitored by UV–vis spectroscopy over 72 h. Figures S1 and S2 indicate that complexes **1** and **2** remain intact in solution, while Figure S3 shows decrease in intensity over time for complex **3** due to precipitation of the compound. Moreover, no isosbestic points were observed indicating that complex **3** is stable in biocompatible media over 72 h. These data are in line with recent findings that metal-arene complexes with this type of coordination mode are resistant to co-ligand(s) exchange for DMSO [26].

2.4. Antiproliferative Activity

The antiproliferative activity of organic species **B**, **HL**¹ and **HL**² and complexes **1–3** was investigated in three human tumor cell lines (lung adenocarcinoma A549, colon adenocarcinoma LS-174 and triple-negative breast adenocarcinoma MDA-MB-231) and one normal human lung fibroblast cell line MRC-5. Cisplatin was used as reference compound. The IC₅₀ values (μM) after 72 h of continuous drug action are summarized in Table 1 and a bar graph plot is shown in Figure S16 (Supplementary Material). All organic compounds are almost nontoxic in A549 cells and revealed low toxicity in LS-174 and MDA-MB-231 cells, which is comparable with that in noncancerous cells MRC-5. Comparison of the IC₅₀ values for **HL**¹ and **HL**² in cancer cell lines suggests that morpholine moiety does not have any effect on the cytotoxicity in cancer cells. Complex formation enhances the antiproliferative activity of **HL**¹ and **HL**² in all cell lines tested. Copper(II) complex **3** exhibited the highest antiproliferative activity in the tested cell lines with lowest IC₅₀ value of 10.9 ± 0.8 μM in LS-174 cells, which is even more effective than cisplatin and showed significant selectivity for this cells line when compared to that in noncancerous cell line (Selectivity Index 2.9), which was superior to that of the reference drug (0.62). Increased cytotoxicity of transition metal complexes in comparison with that of organic ligands is probably due to enhanced mechanisms of cellular uptake via metal-specific transporter proteins, such as transferrin for Ru(II) [37–39], and *Ctr1* or *ATOX1* for Cu(II) [40–43]. In addition, the higher antiproliferative activity of copper(II) complex **3** in comparison to that of the corresponding ligand, as well as to that of ruthenium(II)-*p*-cymene- and osmium(II)-*p*-cymene complexes **1** and **2** is their potential ability of generation ROS via Fenton-like reactions as was observed for other copper(II) complexes with related tridentate ligands [44].

Table 1. Cytotoxic activity of compounds **B**, **HL¹**, **HL²** and **1–3** vs. cisplatin in terms of IC₅₀ values (μM), expressed as mean ± SD of at least two independent experiments performed in triplicates. IC₅₀ values of tested complexes and ligands were determined from dose–response curves after 72 h continuous drug action by MTT assay.

Compound	A549	LS-174	MDA-MB-231	MRC-5
B	157.9 ± 3.7	86.0 ± 0.5	66.7 ± 8.7	99.7 ± 0.3
HL¹	180.7 ± 5.8	84.4 ± 2.1	89.8 ± 1.0	93.5 ± 4.1
HL²	190.2 ± 2.1	98.8 ± 6.6	81.6 ± 8.5	77.3 ± 3.1
1	41.5 ± 2.9	47.7 ± 6.4	65.4 ± 2.5	44.1 ± 5.7
2	50.0 ± 8.9	59.4 ± 2.9	74.4 ± 5.2	69.7 ± 3.0
3	37.2 ± 2.4	10.9 ± 0.8	33.7 ± 5.1	31.8 ± 6.6
Cisplatin	24.7 ± 3.5	23.6 ± 4.4	9.0 ± 0.5	14.6 ± 1.1

To find an explanation for the low cytotoxicity of **B** we looked at docking capability of **B** to PIM-1 enzyme binding pocket. PIM-1 was chosen, since Meggers et al. co-crystallized selected compounds with structures related to Paullones with this proto-oncogene [29], and due to recently published studies, where indolo[2,3-*c*]quinolines and indolo[2,3-*d*]benzazepines modified at the lactam moiety showed strong binding to its ATP-binding pocket [28].

2.5. Molecular Docking of Species **B** to PIM-1

Structures **A** and **B** were docked to the binding sites of PIM-1 (PDB ID: 1YXX, resolution 2.00 Å) [45] kinase. The robustness of the docking scaffold has been previously reported [28]. The GoldScore (GS) [46] and ChemScore(CS) [47,48] ChemPLP (Piecewise Linear Potential) [49] and ASP (Astex Statistical Potential) [50] scoring functions were implemented to predict the binding modes and relative energies of the ligands using the GOLD (v2020.2.0) software suite. The binding scores, for the ligands are given in Table S3 and they have similar scores to the co-crystallized ligand **LI7** [45] indicating reasonable binding. Derivative **B**, with the hydantoin unit, has better scores than species **A** except for CS.

Analysis of the docking revealed that all of the scoring functions predicted the same conformation in the binding pocket except CS for structure **B**. In the case of **A** ASP and PLP predicted the same conformation as for **B** whereas the other two were quite different. Finally, the co-crystallized ligand **LI7** was overlapped with the dominant conformation of **B** as shown in Figure 6A. A very good fit is predicted as seen in Figure 6A as the **B** fully occupies the binding pocket without any clashes with the adjacent amino acid residues. However, no hydrogen bonding is found for the dominant conformation to the neighboring amino acids as shown in Figure 6B. The other conformations were predicted to bind to PIM-1 via hydrogen bonds but consequently had a poorer fit in the pocket.

2.6. Chemical Space

The calculated molecular descriptors MW (molecular weight), log *P* (water-octanol partition coefficient), HD (hydrogen bond donors), HA (hydrogen bond acceptors), PSA (polar surface area) and RB (rotatable bonds) are given in Table S4 derived using the QikProp software [51]. The values for the ligands' descriptors lie mostly within lead- and drug-like chemical space with the notable exception that PSA for species **B**, which is outside the Known Drug Space (KDS) (for the definition of lead-like, drug-like and KDS regions see [52] and Table S5).

The Known Drug Indexes (KDIs) for the species **B** and **A** were calculated to gauge the balance of the molecular descriptors (MW, log*P*, HD, HA, PSA and RB). This method is based on the analysis of drugs in clinical use, i.e., the statistical distribution of each descriptor is fitted to a Gaussian function and normalized to 1 resulting in a weighted

index. Both the summation of the indexes (KDI_{2a}) and multiplication (KDI_{2b}) methods were used [53] as shown for KDI_{2a} in Equation (1) and for KDI_{2b} in Equation (2):

$$KDI_{2a} = I_{MW} + I_{\log P} + I_{HD} + I_{HA} + I_{RB} + I_{PSA} \quad (1)$$

$$KDI_{2b} = I_{MW} \times I_{\log P} \times I_{HD} \times I_{HA} \times I_{RB} \times I_{PSA} \quad (2)$$

The numerical results are given in Table S6 in the Supplementary Material.

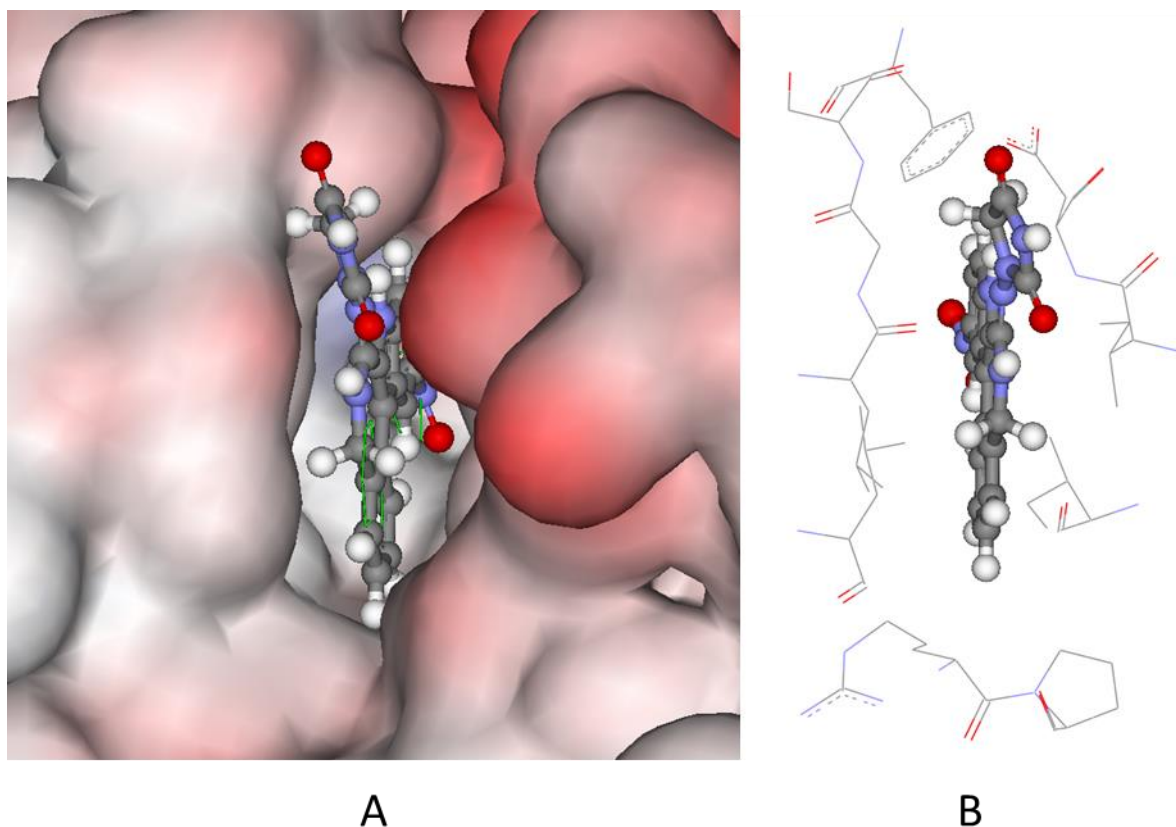


Figure 6. (A) The docked pose of **B** using the ChemPLP scoring function in the PIM-1's binding site, the co-crystallized ligand **LI7** is shown as green sticks, its hydrogens are not shown for clarity. The protein surface is rendered; blue color depicts regions with a partial positive charge on the surface; red color depicts regions with a partial negative charge and grey color shows neutral areas; (B) The predicted binding of species **B**, no hydrogen bonding interactions were predicted. The amino acids making up the docking scaffold are LEU44, GLY45, SER46, PHE49, ILE104, LEU120, ARG122, PRO123, ILE185 and ASP186 within 5 Å.

The KDI_{2a} values for the ligands are 4.92 (**B**) and 5.19 (**A**) with a theoretical maximum of 6 and the average of 4.08 (± 1.27) for known drugs. The KDI_{2b} are 0.20 (**B**) and 0.40 (**A**), with a theoretical maximum of 1 and with KDS average of 0.18 (± 0.20). This means that the molecular descriptors' balance is good resulting in good biocompatibility.

Species **B** contains an imine group, which is quite electron rich rendering it susceptible to an electrophilic attack and a nitro group susceptible for reduction. To test this the ionization potential (one-electron oxidation) and electron affinity (one-electron reduction) were derived for **B** using the density functional theory (DFT) and compared to the statistical distribution of known drugs [54]. The ionization potential is 7.2 eV and 95% of drugs lie in the 6.0–9.0 eV range; the electron affinity is -1.5 eV with drugs in the -1.5 – -2.0 eV range [54]. Thus, **B** is within the ranges of known drugs albeit at the edge of one-electron reduction. Furthermore, **B** has one N–N single bond, which is relatively weak compared to their C–C counterparts. Therefore, the bond dissociation energy (BDE) for the N–N single bond was

also derived using DFT, resulting in 62.7 kcal/mol, which is substantially higher than the average for drugs with N-N bonds (53.9 kcal/mol, $n = 23$) [55].

3. Materials and Methods

1-Aminohydantoin was purchased from abcr. 2-Formylpyridine was bought from Alfa Aesar. The 6-(*N*-methylmorpholine) derivative of 2-formylpyridine was synthesized according to literature [56]. The core structure **A** was synthesized as reported recently [26]. $[\text{RuCl}_2(p\text{-cymene})]_2$ [57] and $[\text{OsCl}_2(p\text{-cymene})]_2$ [58] were synthesized according to published protocols.

3.1. Synthesis of Proligands **HL**¹ and **HL**²

ESI-MS data as well as yields and elemental analyses for **HL**¹ and **HL**², as well as of complexes **1–3** can be found in Supplementary Material (Table S1).

1-((11-nitro-5,8-dihydroindolo[2,3-*d*]benzazepine-7(6*H*)-ylidene)amino)imidazolidine-2,4-dione (**B**)

A suspension of **A** (300 mg, 1.02 mmol) in POCl_3 (30 mL) under inert atmosphere was stirred at 130 °C for 3 h and then cooled to room temperature. The solvent was removed and to the residue dry acetonitrile (90 mL) was added. The suspension was cooled to 0 °C and added dropwise to a slurry of 1-aminohydantoin in dry acetonitrile (90 mL) at 0 °C. The resulting mixture was stirred at 0 °C for 1 h, then at room temperature for 1 h and at 50 °C overnight. The precipitate was filtered off, treated with EtOAc and saturated aqueous solution of NaHCO_3 (100 mL). The organic phase was separated, while the aqueous phase was extracted with EtOAc (2×50 mL). The combined organic phases were dried over MgSO_4 and purified on silica by using DCM:MeOH 93:7 as eluent to give a yellow solid. Yield: 237 mg (60%). ¹H NMR (500 MHz, $\text{DMSO-}d_6$) δ 12.63 (s, 1H), 10.92 (s, 1H), 8.84 (d, $J = 2.0$ Hz, 1H), 8.20 (dd, $J = 9.1, 2.1$ Hz, 1H), 8.06 (t, $J = 5.2$ Hz, 1H), 7.97 (d, $J = 7.6$ Hz, 1H), 7.71 (d, $J = 9.1$ Hz, 1H), 7.59 (t, $J = 7.4$ Hz, 1H), 7.49 (d, $J = 7.2$ Hz, 1H), 7.41 (t, $J = 7.4$ Hz, 1H), 4.10 (s, 4H).

1-((11-amino-5,8-dihydroindolo[2,3-*d*]benzazepine-7(6*H*)-ylidene)amino)imidazolidine-2,4-dione (**C**)

To a solution of **B** (406 mg, 1.32 mmol) in THF (80 mL) Pd/C (0.1 equiv) was added and the solution was stirred under H_2 atmosphere at 3 bar at room temperature for 28 h. The suspension was filtered over Celite and the filtrate was concentrated to give a beige solid. Yield: 370 mg (99%). ¹H NMR (500 MHz, $\text{DMSO-}d_6$) δ 11.42 (s, 1H), 10.80 (s, 1H), 7.87 (d, $J = 7.7$ Hz, 1H), 7.83 (t, $J = 5.3$ Hz, 1H), 7.46 (t, $J = 7.1$ Hz, 1H), 7.40 (d, $J = 7.4$ Hz, 1H), 7.27 (t, $J = 7.9$ Hz, 2H), 7.13 (s, 1H), 6.70 (dd, $J = 8.6, 1.9$ Hz, 1H), 4.75 (s, 2H), 4.04 (s, 4H).

HL¹·1.1H₂O

To species **C** (200 mg, 0.58 mmol) in anoxic ethanol (2 mL) 2-formylpyridine (61 μL , 0.64 mmol) was added. The resulting solution was stirred at 85 °C for 16 h. The precipitate was filtered off after cooling the reaction mixture to room temperature and washed with EtOH (2 mL) and Et₂O (2 mL). The product was dried at 50 °C *in vacuo* to give a light-orange solid. Yield: 180 mg (69%). ¹H NMR (600 MHz, $\text{DMSO-}d_6$) δ 12.50 (s, 1H, H⁸), 8.77 (s, 1H, H²⁰), 8.72 (d, $J = 4.4$ Hz, 1H, H²³), 8.21 (d, $J = 7.9$ Hz, 1H, H²⁶), 8.03 (d, $J = 7.6$ Hz, 1H, H¹), 7.98–7.95 (m, 1H, H²⁵), 7.94 (d, $J = 1.6$ Hz, 1H, H¹²), 7.61 (t, $J = 8.3$ Hz, 2H, H¹⁸, H⁴), 7.59–7.55 (m, 2H, H⁹, H²), 7.52 (ddd, $J = 7.4, 4.8, 1.0$ Hz, 1H, H²⁴), 7.49 (dd, $J = 8.7, 1.9$ Hz, 1H, H¹⁰), 7.38 (t, $J = 7.4$ Hz, 1H, H³), 7.31 (s, 1H, H¹⁸), 4.77 (s, 2H, H⁵), 4.40 (s, 2H, H¹⁶). ¹³C NMR (151 MHz, $\text{DMSO-}d_6$) δ 168.36 (Cq, C¹⁷), 158.62 (CH, C²⁰), 154.43 (Cq, C²¹), 152.24 (Cq, C¹⁵), 149.59 (CH, C²³), 144.11 (Cq, C¹¹), 140.00 (Cq, C⁷), 136.98 (CH, C²⁵), 136.72 (Cq, C^{8a}), 133.18 (Cq, C^{4a}), 133.00 (Cq, C^{12c}), 129.79 (CH, C⁴), 129.12 (CH, C²), 128.43 (CH, C¹), 126.82 (CH, C³), 125.48 (Cq, C^{12a}), 125.27 (CH, C²⁴), 123.53 (Cq, C^{7a}), 120.97 (CH, C²⁶), 118.72 (CH, C¹⁰), 115.99 (Cq, C^{12b}), 113.22 (CH, C⁹), 112.93 (CH, C¹²), 47.79 (CH₂, C¹⁶), 44.70 (CH₂, C⁵). For numbering scheme of **HL**¹ and **HL**² see Figure S1 in Supplementary Material.

HL²·2H₂O

To species **C** (245 mg, 0.68 mmol) in anoxic EtOH (4 mL) 2-formyl-6-morpholinomethylpyridine (154 mg, 0.75 mmol) was added. The solution was stirred at 85 °C for 16 h. The precipitate was filtered off after cooling to room temperature and washed with EtOH (1 mL) and Et₂O (2 mL). The product was dried at 50 °C *in vacuo* to give a light-yellow solid. Yield: 267 mg (71%). ¹H NMR (600 MHz, DMSO-*d*₆) δ 12.48 (s, 1H, H⁸), 8.75 (s, 1H, H²⁰), 8.09 (d, *J* = 7.6 Hz, 1H, H²⁶), 8.04 (d, *J* = 7.7 Hz, 1H, H¹), 7.93 (dd, *J* = 8.7, 4.6 Hz, 2H, H¹², H²⁵), 7.61 (d, *J* = 7.5 Hz, 1H, H⁴), 7.58 (dt, *J* = 7.7, 6.3 Hz, 4H, H², H¹⁸, H⁹, H²⁴), 7.49 (dd, *J* = 8.7, 1.7 Hz, 1H, H¹⁰), 7.38 (t, *J* = 7.4 Hz, 1H, H³), 7.30 (s, 1H, H¹⁸), 4.77 (s, 2H, H⁵), 4.40 (s, 2H, H¹⁶), 3.68 (s, 2H, H²⁷), 3.65–3.58 (m, 4H, H³⁰), 2.45 (s, 4H, H²⁹). ¹³C NMR (151 MHz, DMSO-*d*₆) δ 168.37 (Cq, C¹⁷), 158.57 (CH, C²⁰), 158.34 (Cq, C²³), 153.95 (Cq, C²¹), 152.26 (Cq, C¹⁵), 144.14 (Cq, C¹¹), 140.03 (Cq, C⁷), 137.37 (CH, C²⁵), 136.74 (Cq, C^{8a}), 133.21 (Cq, C^{12c}), 133.00 (Cq, C^{4a}), 129.79 (CH, C⁴), 129.14 (CH, C²), 128.48 (CH, C¹), 126.82 (CH, C³), 125.49 (Cq, C^{12a}), 124.27 (CH, C²⁴), 123.53 (Cq, C^{7a}), 119.49 (CH, C²⁶), 118.86 (CH, C¹⁰), 116.02 (Cq, C^{12b}), 113.21 (CH, C⁹), 112.88 (CH, C¹²), 66.21 (CH₂, C³⁰), 63.92 (CH₂, C²⁷), 53.36 (CH₂, C²⁹), 47.80 (CH₂, C¹⁶), 44.72 (CH₂, C⁵).

3.2. Synthesis of Ru(II)/Os(II) Arene and Cu(II) Complexes

1·2.5H₂O

To a solution of **HL**¹ (53.8 mg, 0.12 mmol) in ⁱPrOH (58 mL) at 60 °C [RuCl₂(*p*-cymene)]₂ (36.7 mg, 60 μMol) in CHCl₃ (400 μL) was added. The solution was stirred at 60 °C for 1 h. The solvent was removed under reduced pressure and the remainder was re-dissolved in MeOH (10 mL). The solution was overlaid with Et₂O (100 mL) and left to stand at 4 °C overnight. The precipitate was filtered off, washed with THF (5 mL) and dried at 50 °C *in vacuo* overnight to give a red-brownish solid. Yield: 83 mg (91%). ¹H NMR (500 MHz, DMSO-*d*₆) δ 12.85 (s, 1H, H⁸), 9.60 (d, *J* = 5.4 Hz, 1H, H²³), 9.05 (s, 1H, H²⁰), 8.41 (s, 1H, H¹²), 8.31 (t, *J* = 7.6 Hz, 1H, H²⁵), 8.27 (d, *J* = 7.3 Hz, 1H, H²⁶), 8.06 (d, *J* = 7.6 Hz, 1H, H¹), 7.92–7.85 (m, 2H, H¹⁰, H²⁴), 7.74 (d, *J* = 8.7 Hz, 1H, H⁹), 7.67 (d, *J* = 7.5 Hz, 1H, H⁴), 7.64 (s, 1H, H¹⁸), 7.60 (t, *J* = 7.5 Hz, 1H, H²), 7.43 (t, *J* = 7.4 Hz, 1H, H³), 7.32 (s, 1H, H¹⁸), 6.10 (d, *J* = 6.2 Hz, 1H, H^{Cy4} or H^{Cy6}), 5.78 (d, *J* = 6.2 Hz, 1H, H^{Cy3} or H^{Cy7}), 5.72 (d, *J* = 6.1 Hz, 1H, H^{Cy4} or H^{Cy6}), 5.56 (d, *J* = 6.1 Hz, 1H, H^{Cy3} or H^{Cy7}), 4.81 (q, *J* = 15.0 Hz, 2H, H⁵), 4.44 (s, 2H, H¹⁶), 2.55 (dt, *J* = 11.1, 5.5 Hz, 1H, H^{Cy8}), 2.18 (s, 3H, H^{Cy1}), 1.01 (dd, *J* = 9.5, 7.0 Hz, 6H, H^{Cy9}). ¹³C NMR (126 MHz, DMSO-*d*₆) δ 168.30 (Cq, C¹⁷), 166.72 (CH, C²⁰), 155.96 (CH, C²³), 154.87 (Cq, C²¹), 152.27 (Cq, C¹⁵), 146.22 (Cq, C¹¹), 139.87 (CH, C²⁵), 139.75 (Cq, C⁷), 137.65 (Cq, C^{8a}), 133.30 (Cq, C^{4a}), 132.85 (Cq, C^{12c}), 130.00 (CH, C⁴), 129.62 (CH, C²⁶), 129.10 (CH, C²), 128.54 (CH, C¹), 128.49 (CH, C²⁴), 127.20 (CH, C³), 124.70 (Cq, C^{12a}), 124.58 (Cq, C^{7a}), 120.37 (CH, C¹⁰), 116.37 (Cq, C^{12b}), 113.48 (CH, C¹²), 113.15 (CH, C⁹), 105.11 (Cq, C^{Cy5}), 103.20 (Cq, C^{Cy2}), 86.70 (CH, C^{Cy4} or C^{Cy6}), 85.73 (CH, C^{Cy4} or C^{Cy6}), 85.28 (CH, C^{Cy3} or C^{Cy7}), 85.19 (CH, C^{Cy3} or C^{Cy7}), 47.82 (CH₂, C¹⁶), 44.71 (CH₂, C⁵), 30.50 (CH, C^{Cy8}), 21.94 (CH₃, C^{Cy9}), 21.45 (CH₃, C^{Cy9}), 18.31 (CH₃, C^{Cy1}). For numbering scheme of complexes **1** and **2** see Figure S2 in Supplementary Material.

2·2.4H₂O

To a solution of **HL**¹ (50.6 mg, 0.11 mmol) in ⁱPrOH (75 mL) at 60 °C [OsCl₂(*p*-cymene)]₂ (44.5 mg, 56 μMol) in CHCl₃ (1 mL) was added. The solution was stirred at 60 °C for 1 h. The solvent was removed under reduced pressure and the crude solid re-dissolved in MeOH (5 mL). The solution was overlaid with Et₂O (50 mL), filtered off, washed with THF (2 mL) and dried at 50 °C *in vacuo* to give a bright orange solid. Yield: 70 mg (76%). ¹H NMR (600 MHz, DMSO-*d*₆) δ 12.84 (s, 1H, H⁸), 9.53 (d, *J* = 5.6 Hz, 1H, H²³), 9.42 (s, 1H, H²⁰), 8.38 (d, *J* = 7.4 Hz, 1H, H²⁶), 8.33 (d, *J* = 1.7 Hz, 1H, H¹²), 8.28 (td, *J* = 7.8, 1.2 Hz, 1H, H²⁵), 8.03 (d, *J* = 7.7 Hz, 1H, H¹), 7.83 (ddd, *J* = 7.5, 5.8, 1.4 Hz, 1H, H²⁴), 7.78 (dd, *J* = 8.8, 2.0 Hz, 1H, H¹⁰), 7.72 (d, *J* = 8.7 Hz, 1H, H⁹), 7.67 (d, *J* = 7.1 Hz, 1H, H⁴), 7.62 (s, 1H, H¹⁸), 7.60–7.56 (m, 1H, H²), 7.42 (dd, *J* = 11.6, 4.2 Hz, 1H, H³), 7.32 (s, 1H, H¹⁸), 6.38 (d, *J* = 5.8 Hz, 1H, H^{Cy4/6}), 5.98 (d, *J* = 5.8 Hz, 1H, H^{Cy3/7}), 5.92 (d, *J* = 5.7 Hz, 1H,

$H^{Cy4/6}$, 5.72 (d, $J = 5.7$ Hz, 1H, $H^{Cy3/7}$), 4.80 (t, $J = 10.4$ Hz, 2H, H^5), 4.43 (s, 2H, H^{18}), 2.43 (dt, $J = 13.8, 6.9$ Hz, 1H, H^{Cy8}), 2.26 (s, 3H, H^{Cy1}), 0.95 (dd, $J = 12.6, 6.9$ Hz, 6H, H^{Cy9}). ^{13}C NMR (151 MHz, DMSO- d_6) δ 168.29 (Cq, C^{17}), 167.60 (CH, C^{20}), 156.20 (Cq, C^{21}), 155.60 (CH, C^{23}), 152.25 (Cq, C^{15}), 146.18 (Cq, C^{11}), 140.01 (CH, C^{25}), 139.72 (Cq, C^7), 137.71 (Cq, C^{8a}), 133.30 (Cq, C^{4a}), 132.79 (Cq, C^{12c}), 130.00 (CH, C^4), 129.48 (CH, C^{26}), 129.37 (CH, C^{24}), 129.06 (CH, C^2), 128.42 (CH, C^1), 127.21 (CH, C^3), 124.63 (Cq, C^{7a}), 124.62 (Cq, C^{12a}), 120.70 (CH, C^{10}), 116.33 (Cq, C^{12b}), 113.88 (CH, C^{12}), 113.13 (CH, C^9), 97.08 (CH, C^{Cy2}), 96.63 (CH, C^{Cy5}), 78.85 (CH, $C^{Cy4/6}$), 77.70 (CH, $C^{Cy4/6}$), 75.85 (CH, $C^{Cy3/7}$), 75.54 (CH, $C^{Cy3/7}$), 47.80 (CH₂, C^{16}), 44.69 (CH₂, C^5), 30.69 (CH, C^{Cy8}), 21.77 (2 \times CH₃, C^{Cy9}), 18.29 (CH₃, C^{Cy1}).

3·H₂O·0.3ⁱPrOH

To a solution of **HL**² (109 mg, 0.2 mmol) in ⁱPrOH (60 mL) at 70 °C CuCl₂·2H₂O (34 mg, 0.2 mmol) in MeOH (200 μ L) was added. The resulting suspension was stirred at reflux for 45 min and left to stand at 4 °C overnight. The precipitate was filtered off and washed with ⁱPrOH (3 mL). The product was dried at 50 °C *in vacuo* to give a light-brown solid. Yield 120 mg (89%) For electron diffraction measurements, nanometer size crystalline complex **3** was generated by slow diffusion of acetonitrile into a concentrated solution of crude **3** in DMF.

3.3. Crystallographic Structure Determination

The measurements were performed on a Bruker D8 Venture diffractometer. Single crystals were positioned at 40 and 35 mm from the detector, and 717 and 1320 frames were measured, each for 10 and 3 s over 0.360° scan, respectively. The data were processed using SAINT software [59]. Crystal data, data collection parameters, and structure refinement details are given in Table S2. The structures were solved by direct methods and refined by full-matrix least-squares techniques. Non-H atoms were refined with anisotropic displacement parameters. H atoms were inserted in calculated positions and refined with a riding model. The following computer programs and hardware were used: structure solution, SHELXS and refinement, SHELXL [60]; molecular diagrams, ORTEP [61]; computer, Intel CoreDuo. CCDC 2219174 (**B**·CH₃OH), 2219175 (**HL**¹·2DMF) and 2218795 (**3**).

3.4. Sample Preparation and Data Collection for Complex **3** by Electron Diffraction

A few dry grains of **3** were provided in a glass vial with about 11 mm diameter (see Figure 7). A TEM copper grid with 3.05 mm diameter and coated with lacey carbon (Ted Pella) was added to the vial. The grid was not glow-discharged before use but used as purchased. The vial was vortexed for 1 min at 3000/s.

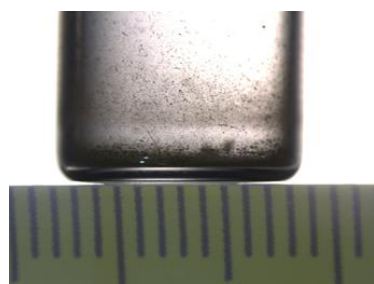


Figure 7. Glass vial of **3** with mm-scale.

The grid was inserted into a Gatan cryo-transfer holder ELSA 698 at room temperature and inserted into a transmission electron microscope JEM2100Plus, JEOL Ltd. (Akishima, Japan). Electron source was a LaB₆ emitter operated at 200 keV. Data were collected with a JUNGFRU detector, 1024 \times 512 pixel [62]. At first, condenser lens aperture 3 and spot size 5 were used. This led to a degradation of the diffraction power during data collection. Consequently, the beam intensity was reduced by setting to the smallest available condenser lens aperture (50 μ m diameter), and the second to weakest spot size (spot size 4 out of

5). Data were collected with a rotation velocity of nominally $0.05^\circ/\text{s}$. Data were collected from 15 crystals (see Figures 8 and 9). Four data sets could be indexed and thus processed (see Figure 10). Data were processed with XDS [63]. Scaling was switched off during data integration [64] and only applied during scaling with XSCALE. Resolution was cut to 0.7 \AA based on $I/\sigma(I) > 1$ and $CC1/2 > 30\%$ [65]. Unit cell parameters suggested a monoclinic lattice, systematic absences suggested space group $P2_1/n$. The structure was solved with SHELXD 2013/2 [60] and refined with SHELXL 2019/1 [66] in kinematic approximation. Scattering factors were fitted in Cromer–Mann parametrization $f(s) = \sum (i = 1..4) a_i \exp(-b_i*s^2) + c$ against the values tabulated in Table 4.2.6.8 of the International Tables of Crystallography, Volume C [67], starting from the parameters published by Peng 1999 [68]. Hydrogen atoms were placed in riding positions at inter-nuclear distances [69]. Geometric 1,2- and 1,3-distance restraints were generated with OPENBABEL [70] and the GRADE-server [71]. Only the ligand was restrained, and the distances listed in the legend to Figure 5 are unrestrained. Unit cell dimensions very optimized against the geometric restraints with CELLOPT [72].

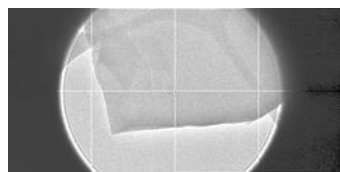


Figure 8. Partial view of the crystal no. 08 at 25,500-fold magnification. Field of view has a diameter of $1.9 \mu\text{M}$.

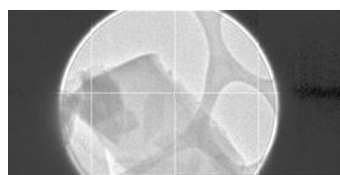


Figure 9. Partial view of crystal no. 13 at 25,500-fold magnification. Field of view has a diameter of $1.9 \mu\text{M}$.

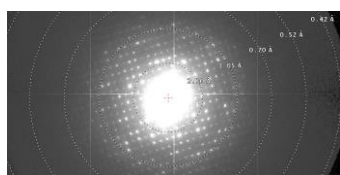


Figure 10. Diffraction image for crystal no. 08. Effective detector distance is 665 mm.

3.5. Cell Culture

All cell lines used in this study were purchased from the American Type Culture Collection (ATCC). The human lung adenocarcinoma (A549, Cat No ATCC[®] CCL-185[™]), human colorectal adenocarcinoma (LS-174, Cat No ATCC[®] CL-188[™]), and normal human lung fibroblast cells (MRC-5, Cat No ATCC[®] CCL-171[™]) were maintained as monolayer culture in the Roswell Park Memorial Institute (RPMI) 1640 nutrient medium (Sigma Chemicals Co., Ltd., Saint Louis, MO, USA.). The human tumor cell line derived from triple-negative caucasian breast adenocarcinoma (MDA-MB-231, Cat No ATCC[®] HTB-26[™]), was maintained in Dulbecco's Modified Eagle's Medium (DMEM) (Sigma Chemicals Co., Ltd., Saint Louis, MO, USA.). Nutrient mediums were prepared in sterile ionized water, supplemented with penicillin (100 IU/mL), streptomycin (200 $\mu\text{g}/\text{mL}$), 4-(2-hydroxyethyl) piperazine-1-ethanesulfonic acid (HEPES) (25 mM), L-glutamine (3 mM) (Sigma Chemicals Co., Ltd., Saint Louis, MO, USA.) and 10% of heat-inactivated fetal calf serum (FCS) (pH 7.2). The cells were grown at 37°C in a humidified atmosphere containing 5% CO_2 .

3.6. MTT-Assay

The cytotoxic activity of the investigated complexes and their corresponding ligands was analyzed in comparison to cisplatin, *cis*-diamminedichloridoplatinum(II) (CDDP) as reference compound, using the 3-(4,5-dimethylthiazol-yl)-2,5-diphenyltetrazolium bromide (MTT, Sigma) assay as previously described [73,74]. Cells were seeded in 96-well culture plates (Thermo Scientific Nunc™, Rochester, NY, USA) at cell densities of 5000 c/w, in a total volume of 100 µL of nutrient medium, and then cultured in 37 °C incubator, in a humidified atmosphere of 5% CO₂. Briefly, 24 h after seeding, cells were exposed to the investigated compounds. The complexes and ligands were dissolved in dimethyl sulfoxide (DMSO) at a concentration of 10 mM immediately prior the use, and afterwards diluted in culture medium to the desired concentrations. The final DMSO concentration never exceeded 1% (*v/v*). After an incubation period of 72 h, 20 µL of MTT solution (5 mg/mL in phosphate buffer, pH 7.2) was added to each well. Samples were incubated at 37 °C for 4 h, in 5% CO₂ incubator, and then 100 µL of 10% sodium dodecyl sulfate (SDS) was added. Absorbance was recorded after 24 h, on an enzyme linked immunosorbent assay (ELISA) reader (Thermo Labsystems Multiskan EX 200–240 V), at the wavelength of 570 nm. The IC₅₀ value, defined as the concentration of the compound causing 50% cell growth inhibition, was determined from the dose response curves.

3.7. Molecular Docking

The ligands were docked against the crystal structures of PIM-1 (PDB ID: 1YXX, resolution 2.00 Å) [45]. The docking center for the binding pockets were defined as the position of the co-crystallized ligand LI7 ((3E)-3-[(4-hydroxyphenyl)imino]-1*H*-indol-2(3*H*)-one) with 10 Å radius. The GoldScore (GS) [46] and ChemScore (CS) [47,48] ChemPLP (Piecewise Linear Potential) [49] and ASP (Astex Statistical Potential) [50] scoring functions were implemented to predict the binding modes and relative energies of the ligands using the GOLD (v2020.2.0) software suite. The GOLD docking algorithm is reported to be an excellent modelling tool [75,76] The Scigress version FJ 2.6 program [77] was used to build the ligands; the MM3 [78–80] force field was applied to identify the global minimum using the CONFLEX method [81] followed by structural optimisation.

The QikProp v6.2 [51] software package was used to calculate the molecular descriptors of the molecules. The reliability of it QikProp established for the calculated descriptors [82]. Furthermore, the Scigress version FJ 2.6 program [77] was used to calculate the molecular descriptors for the complexes. The Known Drug Indexes (KDI) were calculated from the molecular descriptors as described by Eurtivong and Reynisson [53] For application in Excel, columns for each property were created and the following equations used to derive the KDI numbers for each descriptor: KDI MW: =EXP(-((MW-371.76)²)/(2*(112.76²))), KDI Log P: =EXP(-((LogP-2.82)²)/(2*(2.21²))), KDI HD: =EXP(-((HD-1.88)²)/(2*(1.7²))), KDI HA: =EXP(-((HA-5.72)²)/(2*(2.86²))), KDI RB =EXP(-((RB-4.44)²)/(2*(3.55²))), and KDI PSA: =EXP(-((PSA-79.4)²)/(2*(54.16²))). These equations could simply be copied into Excel and the descriptor name (e.g., MW) substituted with the value in the relevant column. To derive KDI_{2A}, this equation was used: =(KDI MW + KDI LogP + KDI HD + KDI HA + KDI RB + KDI PSA) and for KDI_{2B}: =(KDI MW × KDI LogP × KDI HD × KDI HA × KDI RB × KDI PSA).

The Gaussian 16 software suite [83] was used with unrestricted DFT. The B3LYP functional hybrid approach was employed [84–86] and standard 6-31+G(d,p) diffused basis set [87,88] was used for geometry optimization and frequency analysis (keywords: opt freq). The zero-point vibrational energies (ZPE) were scaled according to Wong (0.9804) [89]. In all cases, normal modes revealed no imaginary frequencies indicating that they represent minima on the potential energy surface. The subsequent energy calculations were then performed with the larger 6-311+G(2df, p) basis set. Adiabatic ionization potentials (IP) and adiabatic electron affinities (EA) were calculated as described in Forseman and Frisch [90]. The bond dissociation energies were calculated as in Yu and Reynisson [55]. The energies and ZPA are given in Table S4.

4. Conclusions

Attachment of 1-AH moiety to a latonduine backbone was expected to enhance the docking ability to PIM-1 enzyme by exploiting its potential ability to form hydrogen bonds. Molecular docking calculations revealed that despite good accommodation of species **B** in the binding pocket of PIM-1 the 1-AH moiety is not involved in any hydrogen bonding interactions. Attempts to create a metal-binding site at the backbone of new hybrid molecule via Schiff base condensation reactions resulted in intramolecular cyclization with formation of a triazole ring and a dangling amide functional group with isolation of **HL**¹ and **HL**². By further exploiting their complex formation ability ruthenium(II)- and osmium(II)-arene complexes **1** and **2**, as well as copper(II) complex **3** were synthesized and characterized. For the first time we used electron diffraction for elucidation of molecular structure of a metal complex, which could not be crystallized to give single crystals suitable for routine X-ray diffraction study. Several nanometer size crystals provided electron diffraction data for determination of molecular structure of complex **3**. All the organic compounds tested have not revealed marked cytotoxicity in cancer cell lines. Low antiproliferative activity of species **B** is likely due to large PSA (polar surface area) value lying outside drug-like space. In contrast to previously reported data, indicating that chemical modification of the lactam group at the indolobenzazepine backbone has a favorable effect on cytotoxicity, intramolecular cyclization with formation of a triazole ring fused to the core structure resulted in a marked drop of antiproliferative activity. Coordination of **HL**¹ and **HL**² to ruthenium(II)-, osmium(II)-arene and copper(II), respectively, enhanced markedly their antiproliferative activity. The IC₅₀ values of complexes **1–3** follow the order **2** > **1** > **3**. The most cytotoxic in all three cancer cell lines complex **3**, when compared to **1** and **2**, in addition to the highest antiproliferative activity showed selectivity towards LS-174 cells (when compared to normal cells MRC-5) superior to that of clinical drug cisplatin.

Supplementary Materials: The following supporting information can be downloaded at: <https://www.mdpi.com/article/10.3390/inorganics11010030/s1>, Figure S1: UV-vis absorption spectra of **1** (35 μM) in DMSO/H₂O 1/99 monitored over 72 h; Figure S2: UV-vis absorption spectra of **2** (37 μM) in DMSO/H₂O 1/99 monitored over 72 h; Figure S3: UV-vis absorption spectra of **3** (49 μM) in DMSO/H₂O 1/99 monitored over 72 h; Figures S4–S10: ¹H NMR spectra of **B**, **C**, **C***, **HL**¹, **HL**², **1** and **2**; Figures S11–S14: ¹³C NMR spectra of **HL**¹, **HL**², **1** and **2**; Figure S15: ¹⁵N-¹H HSQC NMR spectrum of **HL**¹; Figure S16: IC₅₀ values (μM) of tested complexes and ligands vs. cisplatin; Figures S17–S23: Positive ion ESI-mass spectra of **B**, **C**, **HL**¹, **HL**², **1–3**; Table S1: Yields and analytical data for **HL**¹ and **HL**², and complexes **1–3**; Table S2: Crystallographic data and refinement details for **B**·CH₃OH, **HL**¹·2DMF and **3**; Table S3: The binding affinities as predicted by the scoring functions for the Pim1 kinase; Table S4: The molecular descriptors for species **A** and **B**; Table S5: Definition of lead-like, drug-like and Known Drug Space (KDS) in terms of molecular descriptors; Table S6: The single point and corrected zero-point vibrational energies (ZPE) of **B**; Scheme S1. Numbering scheme of **HL**¹ and **HL**²; Scheme S2. Numbering scheme for complexes **1** (M = Ru) and **2** (M = Os).

Author Contributions: V.B.A. designed the project. C.W. conducted the synthesis and spectroscopic characterization of the compounds tested. S.A. evaluated the cytotoxicity in vitro. T.G. conducted electron diffraction analysis. A.P.-R. was in charge of SC-XRD experiments. J.R. conducted molecular docking and chemical space calculations. V.B.A. and C.W. wrote the manuscript. All authors have read and agreed to the published version of the manuscript.

Funding: This work was funded by Austrian Science Fund (FWF) via grant number P31293-N37.

Institutional Review Board Statement: Not applicable.

Informed Consent Statement: Not applicable.

Data Availability Statement: The crystallographic data of **B**, **HL**¹ and **3** are provided in Supplementary Material.

Acknowledgments: Austrian Science Fund (FWF) is acknowledged for financial support of this work via grant number P31293-N37. This study was also supported by the Ministry of Education, Science and Technological Development of the Republic of Serbia, grant number 451-03-9/2021-14/200043.

Conflicts of Interest: The authors declare no conflict of interest.

References

1. Cancer over Time. Global Cancer Observatory. Available online: <https://gco.iarc.fr/overtime/en> (accessed on 4 May 2022).
2. Cancer Survival. Global Cancer Observatory. Available online: <https://gco.iarc.fr/survival/survmark/> (accessed on 4 May 2022).
3. Cancer Tomorrow. Global Cancer Observatory. Available online: <https://gco.iarc.fr/tomorrow/en> (accessed on 4 May 2022).
4. Primik, M.F.; Filak, L.K.; Arion, V.B. Metal-Based Indolobenzazepines and Indoloquinolines: From Moderate CDK Inhibitors to Potential Antitumor Drugs. In *Advances in Organometallic Chemistry and Catalysis*; Pombeiro, A.J.L., Ed.; John Wiley & Sons, Inc.: Hoboken, NJ, USA, 2013; pp. 605–617.
5. Primik, M.F.; Mühlgassner, G.; Jakupec, M.A.; Zava, O.; Dyson, P.J.; Arion, V.B.; Keppler, B.K. Highly Cytotoxic Copper(II) Complexes with Modified Paullone Ligands. *Inorg. Chem.* **2010**, *49*, 302–311. [[CrossRef](#)] [[PubMed](#)]
6. Primik, M.F.; Göschl, S.; Jakupec, M.A.; Roller, A.; Keppler, B.K.; Arion, V.B. Structure–Activity Relationships of Highly Cytotoxic Copper(II) Complexes with Modified Indolo[3,2-*c*]quinoline Ligands. *Inorg. Chem.* **2010**, *49*, 11084–11095. [[CrossRef](#)] [[PubMed](#)]
7. Dobrov, A.; Arion, V.B.; Kandler, N.; Ginzinger, W.; Jakupec, M.A.; Ruffińska, A.; Graf von Keyserlingk, N.; Galanski, M.S.; Kowol, C.; Keppler, B.K. The First Metal-Based Paullone Derivative with High Antiproliferative Activity in Vitro. *Inorg. Chem.* **2006**, *45*, 1945–1950. [[CrossRef](#)] [[PubMed](#)]
8. Arion, V.B.; Dobrov, A.; Göschl, S.; Jakupec, M.A.; Keppler, B.K.; Rapta, P. Ruthenium- and Osmium-Arene-Based Paullones Bearing a TEMPO Free-Radical Unit as Potential Anticancer Drugs. *Chem. Commun.* **2012**, *48*, 8559–8561. [[CrossRef](#)] [[PubMed](#)]
9. Schultz, C.; Link, A.; Leost, M.; Zaharevitz, D.W.; Gussio, R.; Sausville, E.A.; Meijer, L.; Kunick, C. Paullones, a Series of Cyclin-Dependent Kinase Inhibitors: Synthesis, Evaluation of CDK1/Cyclin B Inhibition, and in Vitro Antitumor Activity. *J. Med. Chem.* **1999**, *42*, 2909–2919. [[CrossRef](#)]
10. Knockaert, M.; Wieking, K.; Schmitt, S.; Leost, M.; Grant, K.M.; Mottram, J.C.; Kunick, C.; Meijer, L. Intracellular Targets of Paullones. *J. Biol. Chem.* **2002**, *277*, 25493–25501. [[CrossRef](#)]
11. Kunick, C.; Lauenroth, K.; Wieking, K.; Xie, X.; Schultz, C.; Gussio, R.; Zaharevitz, D.; Leost, M.; Meijer, L.; Weber, A.; et al. Evaluation and Comparison of 3D-QSAR CoMSIA Models for CDK1, CDK5, and GSK-3 Inhibition by Paullones. *J. Med. Chem.* **2004**, *47*, 22–36. [[CrossRef](#)]
12. Kunick, C.; Zeng, Z.; Gussio, R.; Zaharevitz, D.; Leost, M.; Totzke, F.; Schächtele, C.; Kubbutat, M.H.G.; Meijer, L.; Lemcke, T. Structure-Aided Optimization of Kinase Inhibitors Derived from Alsterpaullone. *ChemBioChem* **2005**, *6*, 541–549. [[CrossRef](#)]
13. Leost, M.; Schultz, C.; Link, A.; Wu, Y.-Z.; Biernat, J.; Mandelkow, E.-M.; Bibb, J.A.; Snyder, G.L.; Greengard, P.; Zaharevitz, D.W.; et al. Paullones Are Potent Inhibitors of Glycogen Synthase Kinase-3 β and Cyclin-Dependent Kinase 5/P25: Paullones Inhibit GSK-3 β and CDK5/P25. *Eur. J. Biochem.* **2000**, *267*, 5983–5994. [[CrossRef](#)]
14. Zaharevitz, D.W.; Gussio, R.; Leost, M.; Senderowicz, A.M.; Lahusen, T.; Kunick, C.; Meijer, L.; Sausville, E.A. Discovery and Initial Characterization of the Paullones, a Novel Class of Small-Molecule Inhibitors of Cyclin-Dependent Kinases. *Cancer Res.* **1999**, *59*, 2566–2569.
15. Soto, S.; Vaz, E.; Dell’Aversana, C.; Álvarez, R.; Altucci, L.; de Lera, Á.R. New Synthetic Approach to Paullones and Characterization of Their SIRT1 Inhibitory Activity. *Org. Biomol. Chem.* **2012**, *10*, 2101–2112. [[CrossRef](#)]
16. Bain, J.; Plater, L.; Elliott, M.; Shpiro, N.; Hastie, C.J.; Mclauchlan, H.; Klevernic, I.; Arthur, J.S.C.; Alessi, D.R.; Cohen, P. The Selectivity of Protein Kinase Inhibitors: A Further Update. *Biochem. J.* **2007**, *408*, 297–315. [[CrossRef](#)] [[PubMed](#)]
17. Bain, J.; Mclauchlan, H.; Elliott, M.; Cohen, P. The Specificities of Protein Kinase Inhibitors: An Update. *Biochem. J.* **2003**, *371*, 199–204. [[CrossRef](#)] [[PubMed](#)]
18. Lington, R.G.; Williams, D.E.; Tahir, A.; Van Soest, R.; Andersen, R.J. Latonduines A and B, New Alkaloids Isolated from the Marine Sponge *Stylissa Carteri*: Structure Elucidation, Synthesis, and Biogenetic Implications. *Org. Lett.* **2003**, *5*, 2735–2738. [[CrossRef](#)] [[PubMed](#)]
19. Fouad, M.A.; Debbab, A.; Wray, V.; Müller, W.E.G.; Proksch, P. New Bioactive Alkaloids from the Marine Sponge *Stylissa* sp. *Tetrahedron* **2012**, *68*, 10176–10179. [[CrossRef](#)]
20. Putey, A.; Joucla, L.; Picot, L.; Besson, T.; Joseph, B. Synthesis of Latonduine Derivatives via Intramolecular Heck Reaction. *Tetrahedron* **2007**, *63*, 867–879. [[CrossRef](#)]
21. Wan, Y.; Li, Y.; Yan, C.; Yan, M.; Tang, Z. Indole: A Privileged Scaffold for the Design of Anti-Cancer Agents. *Eur. J. Med. Chem.* **2019**, *183*, 111691. [[CrossRef](#)]
22. Brancale, A.; Silvestri, R. Indole, a Core Nucleus for Potent Inhibitors of Tubulin Polymerization. *Med. Res. Rev.* **2007**, *27*, 209–238. [[CrossRef](#)]
23. Singh, A.K.; Raj, V.; Saha, S. Indole-Fused Azepines and Analogues as Anticancer Lead Molecules: Privileged Findings and Future Directions. *Eur. J. Med. Chem.* **2017**, *142*, 244–265. [[CrossRef](#)]
24. Putey, A.; Popowycz, F.; Do, Q.T.; Bernard, P.; Talapatra, S.K.; Kozielski, F.; Galmarini, C.M.; Joseph, B. Indolobenzazepin-7-ones and 6-, 8-, and 9-Membered Ring Derivatives as Tubulin Polymerization Inhibitors: Synthesis and Structure-Activity Relationship Studies. *J. Med. Chem.* **2009**, *52*, 5916–5925. [[CrossRef](#)]

25. Filak, L.K.; Mühlgassner, G.; Jakupec, M.A.; Heffeter, P.; Berger, W.; Arion, V.B.; Keppler, B.K. Organometallic Indolo[3,2-*c*]quinolines versus Indolo[3,2-*d*]benzazepines: Synthesis, Structural and Spectroscopic Characterization, and Biological Efficacy. *J. Biol. Inorg. Chem.* **2010**, *15*, 903–918. [[CrossRef](#)] [[PubMed](#)]
26. Wittmann, C.; Sivchenko, A.S.; Bacher, F.; Tong, K.K.H.; Guru, N.; Wilson, T.; Gonzales, J.; Rauch, H.; Kossatz, S.; Reiner, T.; et al. Inhibition of Microtubule Dynamics in Cancer Cells by Indole-Modified Latonduine Derivatives and Their Metal Complexes. *Inorg. Chem.* **2022**, *61*, 1456–1470. [[CrossRef](#)] [[PubMed](#)]
27. Bacher, F.; Wittmann, C.; Nové, M.; Spengler, G.; Marć, M.A.; Enyedy, E.A.; Darvasiová, D.; Rapta, P.; Reiner, T.; Arion, V.B. Novel Latonduine Derived Proligands and Their Copper(II) Complexes Show Cytotoxicity in the Nanomolar Range in Human Colon Adenocarcinoma Cells and *in Vitro* Cancer Selectivity. *Dalton Trans.* **2019**, *48*, 10464–10478. [[CrossRef](#)] [[PubMed](#)]
28. Wittmann, C.; Bacher, F.; Enyedy, E.A.; Dömötör, O.; Spengler, G.; Madejski, C.; Reynisson, J.; Arion, V.B. Highly Antiproliferative Latonduine and Indolo[2,3-*c*]quinoline Derivatives: Complex Formation with Copper(II) Markedly Changes the Kinase Inhibitory Profile. *J. Med. Chem.* **2022**, *65*, 2238–2261. [[CrossRef](#)]
29. Anand, R.; Maksimoska, J.; Pagano, N.; Wong, E.Y.; Gimotty, P.A.; Diamond, S.L.; Meggers, E.; Marmorstein, R. Toward the Development of a Potent and Selective Organoruthenium Mammalian Sterile 20 Kinase Inhibitor. *J. Med. Chem.* **2009**, *52*, 1602–1611. [[CrossRef](#)]
30. Puszyńska-Tuszkaw, M.; Daszkiewicz, M.; Maciejewska, G.; Adach, A.; Cieślak-Golonka, M. Interaction of Hydantoin with Transition Metal Ions: Synthesis, Structural, Spectroscopic, Thermal and Magnetic Properties of $[M(H_2O)_4(Phenyltoinate)_2]$ $M = Ni(II), Co(II)$. *Struct. Chem.* **2010**, *21*, 315–321. [[CrossRef](#)]
31. Rajic, Z.; Zorc, B.; Raic-Malic, S.; Ester, K.; Kralj, M.; Pavelic, K.; Balzarini, J.; De Clercq, E.; Mintas, M. Hydantoin Derivatives of L- and D-Amino Acids: Synthesis and Evaluation of Their Antiviral and Antitumoral Activity. *Molecules* **2006**, *11*, 837–848. [[CrossRef](#)]
32. Levo, Y.; Trainin, N. Hydantoin Immunosuppression and Carcinogenesis. *Clinical Exp. Immunol.* **1975**, *19*, 521–527.
33. Cavazzoni, A.; Alfieri, R.R.; Carmi, C.; Zuliani, V.; Galetti, M.; Fumarola, C.; Frazzi, R.; Bonelli, M.; Bordi, F.; Lodola, A.; et al. Dual Mechanisms of Action of the 5-Benzylidene-Hydantoin UPR1024 on Lung Cancer Cell Lines. *Mol. Cancer Ther.* **2008**, *7*, 361–370. [[CrossRef](#)]
34. Carmi, C.; Cavazzoni, A.; Zuliani, V.; Lodola, A.; Bordi, F.; Plazzi, P.V.; Alfieri, R.R.; Petronini, P.G.; Mor, M. 5-Benzylidene-Hydantoin as New EGFR Inhibitors with Antiproliferative Activity. *Bioorg. Med. Chem. Lett.* **2006**, *16*, 4021–4025. [[CrossRef](#)]
35. Primik, M.F.; Göschl, S.; Meier, S.M.; Eberherr, N.; Jakupec, M.A.; Enyedy, É.A.; Novitchi, G.; Arion, V.B. Dicopper(II) and Dizinc(II) Complexes with Nonsymmetric Dinucleating Ligands Based on Indolo[3,2-*c*]quinolines: Synthesis, Structure, Cytotoxicity, and Intracellular Distribution. *Inorg. Chem.* **2013**, *52*, 10137–10146. [[CrossRef](#)] [[PubMed](#)]
36. Addison, A.W.; Rao, T.N.; Reedijk, J.; van Rijn, J.; Verschoor, G.C. Synthesis, Structure, and Spectroscopic Properties of Copper(II) Compounds Containing Nitrogen–Sulphur Donor Ligands; the Crystal and Molecular Structure of Aqua[1,7-bis(*N*-methylbenzimidazol-2'-yl)-2,6-dithiaheptane]copper(II) perchlorate. *J. Chem. Soc. Dalton Trans.* **1984**, 1349–1356. [[CrossRef](#)]
37. Jungwirth, U.; Kowol, C.; Keppler, B.; Hartinger, C.; Berger, W.; Heffeter, P. Anticancer Activity of Metal Complexes: Involvement of Redox Processes. *Antioxid. Redox Signal.* **2011**, *15*, 1085–1127. [[CrossRef](#)] [[PubMed](#)]
38. Riccardi, C.; Musumeci, D.; Irace, C.; Paduano, L.; Montesarchio, D. Ru^{III} Complexes for Anticancer Therapy: The Importance of Being Nucleolipidic. *Eur. J. Org. Chem.* **2017**, *7*, 1100–1119. [[CrossRef](#)]
39. Thota, S.; Rodrigues, D.; Crans, D.; Barreiro, E.J. $Ru(II)$ Compounds: Next-Generation Anticancer Metallotherapeutics? *J. Med. Chem.* **2018**, *61*, 5805–5821. [[CrossRef](#)] [[PubMed](#)]
40. Shanbhag, V.C.; Gudekar, N.; Jasmer, K.; Papageorgiou, C.; Singh, K.; Petris, M. Copper metabolism as a unique vulnerability in cancer. *Biochim. Biophys. Acta Mol. Cell Res.* **2021**, *1868*, 118893. [[CrossRef](#)] [[PubMed](#)]
41. Denoyer, D.; Masaldan, S.; La Fontaine, S.; Cater, M. Targeting copper in cancer therapy: 'Copper That Cancer'. *Metallomics* **2015**, *7*, 1459–1476. [[CrossRef](#)] [[PubMed](#)]
42. Babak, M.V.; Ahn, D. Modulation of Intracellular Copper Levels as the Mechanism of Action of Anticancer Copper Complexes: Clinical Relevance. *Biomedicines* **2021**, *9*, 852. [[CrossRef](#)]
43. da Silva, D.A.; De Luca, A.; Squitti, R.; Rongioletti, M.; Rossi, L.; Machado, C.; Cerchiaro, G.J. Copper in tumors and the use of copper-based compounds in cancer treatment. *J. Inorg. Biochem.* **2022**, *226*, 111634. [[CrossRef](#)]
44. Dobrov, A.; Göschl, S.; Jakupec, M.A.; Popović-Bijelić, A.; Gräslund, A.; Rapta, P.; Arion, V.B. A Highly Cytotoxic Modified Paullone Ligand Bearing a TEMPO Free-Radical Unit and Its Copper(II) Complex as Potential HR2 RNR Inhibitors. *Chem. Commun.* **2013**, *49*, 10007–10009. [[CrossRef](#)]
45. Kumar, A.; Mandiyan, V.; Suzuki, Y.; Zhang, C.; Rice, J.; Tsai, J.; Artis, D.R.; Ibrahim, P.; Bremer, R. Crystal Structures of Proto-Oncogene Kinase Pim1: A Target of Aberrant Somatic Hypermutations in Diffuse Large Cell Lymphoma. *J. Mol. Biol.* **2005**, *348*, 183–193. [[CrossRef](#)] [[PubMed](#)]
46. Jones, G.; Willett, P.; Glen, R.C.; Leach, A.R.; Taylor, R. Development and Validation of a Genetic Algorithm for Flexible Docking 1. *J. Mol. Biol.* **1997**, *267*, 727–748. [[CrossRef](#)] [[PubMed](#)]
47. Eldridge, M.D.; Murray, C.W.; Auton, T.R.; Paolini, G.V.; Mee, R.P. Empirical Scoring Functions: I. The Development of a Fast Empirical Scoring Function to Estimate the Binding Affinity of Ligands in Receptor Complexes. *J. Comput. Aided Mol. Des.* **1997**, *11*, 425–445. [[CrossRef](#)] [[PubMed](#)]

48. Verdonk, M.L.; Cole, J.C.; Hartshorn, M.J.; Murray, C.W.; Taylor, R.D. Improved Protein-Ligand Docking Using GOLD. *Proteins Struct. Funct. Bioinform.* **2003**, *52*, 609–623. [CrossRef] [PubMed]
49. Korb, O.; Stützle, T.; Exner, T.E. Empirical Scoring Functions for Advanced Protein–Ligand Docking with PLANTS. *J. Chem. Inf. Model.* **2009**, *49*, 84–96. [CrossRef]
50. Mooij, W.T.M.; Verdonk, M.L. General and Targeted Statistical Potentials for Protein-Ligand Interactions. *Proteins Struct. Funct. Bioinform.* **2005**, *61*, 272–287. [CrossRef]
51. *QikProp*, v6.2; Schrödinger, LLC: New York, NY, USA, 2009.
52. Zhu, F.; Logan, G.; Reynisson, J. Wine Compounds as a Source for HTS Screening Collections. A Feasibility Study. *Mol. Inform.* **2012**, *31*, 847–855. [CrossRef]
53. Eurtivong, C.; Reynisson, J. The Development of a Weighted Index to Optimise Compound Libraries for High Throughput Screening. *Mol. Inform.* **2019**, *38*, 1800068. [CrossRef]
54. Matuszek, A.M.; Reynisson, J. Defining Known Drug Space Using DFT. *Mol. Inform.* **2016**, *35*, 46–53. [CrossRef]
55. Yu, B.; Reynisson, J. Bond Stability of the “Undesirable” Heteroatom–Heteroatom Molecular Moieties for High-Throughput Screening Libraries. *Eur. J. Med. Chem.* **2011**, *46*, 5833–5837. [CrossRef]
56. Ohui, K.; Afanasenko, E.; Bacher, F.; Ting, R.L.X.; Zafar, A.; Blanco-Cabra, N.; Torrents, E.; Dömötör, O.; May, N.V.; Darvasiova, D.; et al. New Water-Soluble Copper(II) Complexes with Morpholine–Thiosemicarbazone Hybrids: Insights into the Anticancer and Antibacterial Mode of Action. *J. Med. Chem.* **2019**, *62*, 512–530. [CrossRef] [PubMed]
57. Bennett, M.A.; Smith, A.K. Arene Ruthenium(II) Complexes Formed by Dehydrogenation of Cyclohexadienes with Ruthenium(III) Trichloride. *J. Chem. Soc. Dalton Trans.* **1974**, 233–241. [CrossRef]
58. Kiel, W.A.; Ball, R.G.; Graham, W.A.G. Carbonyl- η -hexamethylbenzene Complexes of Osmium. Carbon-Hydrogen Activation by (η -C₆Me₆)Os(CO)(H)₂. *J. Organomet. Chem.* **1990**, *383*, 481–496. [CrossRef]
59. *SAINT-Plus*, v8.38A; Bruker-Nonius AXS Inc.: Madison, WI, USA, 2016.
60. Sheldrick, G.M. A Short History of SHELX. *Acta Crystallogr. A* **2008**, *64*, 112–122. [CrossRef] [PubMed]
61. Burnett, M.N.; Johnson, C.K. ORTEP-III: Oak Ridge Thermal Ellipsoid Plot Program for Crystal Structure Illustrations. ORNL-6895, Oak Ridge, Tennessee 37831, U.S. 1996.
62. Fröjdh, E.; Wennmacher, J.; Rzepka, P.; Mozzanica, A.; Redford, S.; Schmitt, B.; van Bokhoven, J.; Gruene, T. Discrimination of Aluminum from Silicon by Electron Crystallography with the JUNGFRU Detector. *Crystals* **2020**, *10*, 1148. [CrossRef]
63. Kabsch, W. XDS. *Acta Crystallogr. D Biol. Crystallogr.* **2010**, *66*, 125–132. [CrossRef]
64. Assmann, G.M.; Wang, M.; Diederichs, K. Making a Difference in Multi-Data-Set Crystallography: Simple and Deterministic Data-Scaling/Selection Methods. *Acta Crystallogr. Sect. Struct. Biol.* **2020**, *76*, 636–652. [CrossRef]
65. Karplus, P.A.; Diederichs, K. Linking Crystallographic Model and Data Quality. *Science* **2012**, *336*, 1030–1033. [CrossRef]
66. Sheldrick, G.M. Crystal Structure Refinement with SHELXL. *Acta Crystallogr. Sect. C Struct. Chem.* **2015**, *71*, 3–8. [CrossRef]
67. Janssen, T.; Janner, A.; Looijenga-Vosb, A.; de Wolff, P.M. (Eds.) *International Tables for Crystallography: Mathematical, Physical and Chemical Tables*, 1st ed.; International Union of Crystallography: Chester, UK, 2006; Volume C.
68. Peng, L.-M. Electron Atomic Scattering Factors and Scattering Potentials of Crystals. *Micron* **1999**, *30*, 625–648. [CrossRef]
69. Gruene, T.; Hahn, H.W.; Luebben, A.V.; Meilleur, F.; Sheldrick, G.M. Refinement of Macromolecular Structures against Neutron Data with SHELXL2013. *J. Appl. Crystallogr.* **2014**, *47*, 462–466. [CrossRef] [PubMed]
70. O’Boyle, N.M.; Banck, M.; James, C.A.; Morley, C.; Vandermeersch, T.; Hutchison, G.R. Open Babel: An Open Chemical Toolbox. *J. Cheminf.* **2011**, *3*, 33. [CrossRef] [PubMed]
71. Smart, O.S.; Sharff, A.; Holstein, J.; Womack, T.O.; Flensburg, C.; Keller, P.; Paciorek, W.; Vornrhein, C.; Bricogne, G. Grade2. Version 1.3.0. Global Phasing Ltd.: Cambridge, UK, 2021.
72. Gruene, T.; Clabbers, M.T.B.; Luebben, J.; Chin, J.M.; Reithofer, M.R.; Stowasser, F.; Alker, A.M. CELLOPT: Improved Unit-Cell Parameters for Electron Diffraction Data of Small-Molecule Crystals. *J. Appl. Crystallogr.* **2022**, *55*, 647–655. [CrossRef] [PubMed]
73. Supino, R. MTT Assays. In *In Vitro Toxicity Testing Protocols*; O’Hare, S., Atterwill, C.K., Eds.; Humana Press: Totowa, NJ, USA, 1995; pp. 137–149.
74. Pavlović, M.; Nikolić, S.; Gligorijević, N.; Dojčinović, B.; Arandelović, S.; Grgurić-Šipka, S.; Radulović, S. New Organoruthenium Compounds with Pyrido[2',3':5,6]pyrazino[2,3-f][1,10]phenanthroline: Synthesis, Characterization, Cytotoxicity, and Investigation of Mechanism of Action. *J. Biol. Inorg. Chem.* **2019**, *24*, 297–310. [CrossRef]
75. Wang, Z.; Sun, H.; Yao, X.; Li, D.; Xu, L.; Li, Y.; Tian, S.; Hou, T. Comprehensive Evaluation of Ten Docking Programs on a Diverse Set of Protein-Ligand Complexes: The Prediction Accuracy of Sampling Power and Scoring Power. *Phys. Chem. Chem. Phys.* **2016**, *18*, 12964–12975. [CrossRef]
76. Bissantz, C.; Folkers, G.; Rognan, D. Protein-Based Virtual Screening of Chemical Databases. 1. Evaluation of Different Docking/Scoring Combinations. *J. Med. Chem.* **2000**, *43*, 4759–4767. [CrossRef]
77. *Scigress Ultra*, V. F.J 2.6. Fujitsu Limited. 2016. Available online: <http://www.scigress.com> (accessed on 14 November 2022).
78. Allinger, N.L.; Yuh, Y.H.; Lii, J.H. Molecular Mechanics. The MM3 Force Field for Hydrocarbons. 1. *J. Am. Chem. Soc.* **1989**, *111*, 8551–8566. [CrossRef]
79. Lii, J.H.; Allinger, N.L. Molecular Mechanics. The MM3 Force Field for Hydrocarbons. 2. Vibrational Frequencies and Thermodynamics. *J. Am. Chem. Soc.* **1989**, *111*, 8566–8575. [CrossRef]

80. Lii, J.H.; Allinger, N.L. Molecular Mechanics. The MM3 Force Field for Hydrocarbons. 3. The van Der Waals' Potentials and Crystal Data for Aliphatic and Aromatic Hydrocarbons. *J. Am. Chem. Soc.* **1989**, *111*, 8576–8582. [[CrossRef](#)]
81. Gotō, H.; Ōsawa, E. An Efficient Algorithm for Searching Low-Energy Conformers of Cyclic and Acyclic Molecules. *J. Chem. Soc. Perkin Trans.* **1993**, *2*, 187–198. [[CrossRef](#)]
82. Ioakimidis, L.; Thoukydidis, L.; Mirza, A.; Naeem, S.; Reynisson, J. Benchmarking the Reliability of QikProp. Correlation between Experimental and Predicted Values. *QSAR Comb. Sci.* **2008**, *27*, 445–456. [[CrossRef](#)]
83. Frisch, M.J.; Trucks, G.W.; Schlegel, H.B.; Scuseria, G.E.; Robb, M.A.; Cheeseman, J.R.; Scalmani, G.; Barone, V.; Petersson, G.A.; Nakatsuji, H.; et al. *Gaussian 16*, Revision C.01. 2019; Gaussian Inc.: Wallingford, CT, USA.
84. Becke, A.D. Density-Functional Exchange-Energy Approximation with Correct Asymptotic Behavior. *Phys. Rev. A* **1988**, *38*, 3098–3100. [[CrossRef](#)] [[PubMed](#)]
85. Becke, A.D. Density-functional Thermochemistry. III. The Role of Exact Exchange. *J. Chem. Phys.* **1993**, *98*, 5648–5652. [[CrossRef](#)]
86. Lee, C.; Yang, W.; Parr, R.G. Development of the Colle-Salvetti Correlation-Energy Formula into a Functional of the Electron Density. *Phys. Rev. B* **1988**, *37*, 785–789. [[CrossRef](#)]
87. Frisch, M.J.; Pople, J.A.; Binkley, J.S. Self-Consistent Molecular Orbital Methods 25. Supplementary Functions for Gaussian Basis Sets. *J. Chem. Phys.* **1984**, *80*, 3265–3269. [[CrossRef](#)]
88. Hariharan, P.C.; Pople, J.A. The Influence of Polarization Functions on Molecular Orbital Hydrogenation Energies. *Theoret. Chim. Acta* **1973**, *28*, 213–222. [[CrossRef](#)]
89. Wong, M.W. Vibrational Frequency Prediction Using Density Functional Theory. *Chem. Phys. Lett.* **1996**, *256*, 391–399. [[CrossRef](#)]
90. Frisch, A.; Foresman, J. *Exploring Chemistry with Electronic Structure Methods*, 3rd ed.; Gaussian Inc.: Wallingford, CT, USA, 1996.

Disclaimer/Publisher's Note: The statements, opinions and data contained in all publications are solely those of the individual author(s) and contributor(s) and not of MDPI and/or the editor(s). MDPI and/or the editor(s) disclaim responsibility for any injury to people or property resulting from any ideas, methods, instructions or products referred to in the content.